Article

A lanthanide-rich kilonova in the aftermath of a long gamma-ray burst

Yu-Han Yang[1]✉, Eleonora Troja[1,2]✉, Brendan O'Connor[3,4,5], Chris L. Fryer[6,7,8,9,10], Myungshin Im[11], Joe Durbak[4,5], Gregory S. H. Paek[11], Roberto Ricci[12,13], Clécio R. Bom[14,15], James H. Gillanders[1], Alberto J. Castro-Tirado[16,17], Zong-Kai Peng[18,19], Simone Dichiara[20], Geoffrey Ryan[21], Hendrik van Eerten[22], Zi-Gao Dai[23], Seo-Won Chang[11], Hyeonho Choi[11], Kishalay De[24], Youdong Hu[16], Charles D. Kilpatrick[25], Alexander Kutyrev[4,5], Mankeun Jeong[11], Chung-Uk Lee[26], Martin Makler[14,27], Felipe Navarete[28] & Ignacio Pérez-García[16]

Observationally, kilonovae are astrophysical transients powered by the radioactive decay of nuclei heavier than iron, thought to be synthesized in the merger of two compact objects[1–4]. Over the first few days, the kilonova evolution is dominated by a large number of radioactive isotopes contributing to the heating rate[2,5]. On timescales of weeks to months, its behaviour is predicted to differ depending on the ejecta composition and the merger remnant[6–8]. Previous work has shown that the kilonova associated with gamma-ray burst 230307A is similar to kilonova AT2017gfo (ref. 9), and mid-infrared spectra revealed an emission line at 2.15 micrometres that was attributed to tellurium. Here we report a multi-wavelength analysis, including publicly available James Webb Space Telescope data[9] and our own Hubble Space Telescope data, for the same gamma-ray burst. We model its evolution up to two months after the burst and show that, at these late times, the recession of the photospheric radius and the rapidly decaying bolometric luminosity ($L_{bol} \propto t^{-2.7\pm0.4}$, where t is time) support the recombination of lanthanide-rich ejecta as they cool.

An extremely bright burst, dubbed gamma-ray burst (GRB) 230307A, triggered the Gamma-ray Burst Monitor aboard NASA's Fermi mission at 15:44:06.67 UTC on 7 March 2023 (hereafter T_0). Observationally, GRB 230307A stands out from the general population of long GRBs for three properties: a record-setting gamma-ray fluence[10] (about 3×10^{-3} erg cm^{-2}; 10–1,000 keV), a weak X-ray counterpart (Fig. 1f) and a strong blue-to-red colour evolution.

Early observations at optical and near-infrared (NIR) wavelengths identify a weak counterpart, whose brightness ($H \approx 20.2$ AB mag at $T_0 + 1.2$ d) matches the extrapolation of the X-ray spectrum. The spectral energy distribution (SED) of the GRB counterpart thus does not show evidence for absorption by gas and dust along the sightline (Methods). After $T_0 + 4$ d, the X-ray and optical emission decay quickly, with temporal power-law indices $\alpha_X = 1.71 \pm 0.10$ and $\alpha_O = 2.64^{+0.16}_{-0.26}$, respectively. Instead, the NIR emission persists for several days after the explosion (K-band magnitude $K \approx 22$ AB mag at $T_0 + 7$ d) and then rapidly declines (Extended Data Fig. 1). Late-time (about $T_0 + 29$ d) observations with the Hubble Space Telescope (HST) and the James Webb Space Telescope (JWST)[9] show that the peak of the NIR emission shifts from about 22,000 Å at $T_0 + 7$ d to ≥44,000 Å at $T_0 + 29$ d. At this time (about $T_0 + 29$ d), the continuum is adequately described by the superposition of a power-law spectrum with spectral index $\beta_{OX} \approx 0.6$ and a blackbody spectrum with temperature $T \approx 638$ K (observer frame; Methods).

The key ingredient to interpret these observations is the GRB distance scale. Unfortunately, in the case of GRB 230307A, no direct redshift measurement is available. Our analysis of the photometric dataset provides evidence for a redshift $z \lesssim 3.3$ (at the 95% confidence level (CL); Methods). This leaves a range of possible distance scales that is still too broad. An alternative route to estimate the GRB's distance is to identify its host galaxy using probabilistic arguments[11]. In the case of GRB 230307A, this methodology leads to several possible host galaxies: (1) a distant ($z \gtrsim 3.9$) star-forming galaxy (G* in Fig. 1e); (2) a

[1]Department of Physics, University of Rome "Tor Vergata", Rome, Italy. [2]INAF - Istituto Nazionale di Astrofisica, Rome, Italy. [3]Department of Physics, The George Washington University, Washington DC, USA. [4]Department of Astronomy, University of Maryland, College Park, MD, USA. [5]Astrophysics Science Division, NASA Goddard Space Flight Center, Greenbelt, MD, USA. [6]Computer, Computational, and Statistical Sciences Division, Los Alamos National Laboratory, Los Alamos, NM, USA. [7]Center for Theoretical Astrophysics, Los Alamos National Laboratory, Los Alamos, NM, USA. [8]The University of Arizona, Tucson, AZ, USA. [9]Department of Physics and Astronomy, The University of New Mexico, Albuquerque, NM, USA. [10]The George Washington University, Washington DC, USA. [11]SNU Astronomy Research Center, Astronomy Program, Department of Physics and Astronomy, Seoul National University, Seoul, Republic of Korea. [12]Istituto Nazionale di Ricerca Metrologica, Turin, Italy. [13]INAF - Istituto di Radioastronomia, Bologna, Italy. [14]Centro Brasileiro de Pesquisas Físicas, Rio de Janeiro, Brazil. [15]Centro Federal de Educação Tecnológica Celso Suckow da Fonseca, Rodovia Mário Covas, Itaguaí, Brazil. [16]Instituto de Astrofísica de Andalucía (IAA-CSIC), Granada, Spain. [17]Unidad Asociada al CSIC Departamento de Ingeniería de Sistemas y Automática, Escuela de Ingenierías Industriales, Universidad de Málaga, Málaga, Spain. [18]Institute for Frontier in Astronomy and Astrophysics, Beijing Normal University, Beijing, China. [19]Department of Astronomy, Beijing Normal University, Beijing, China. [20]Department of Astronomy and Astrophysics, The Pennsylvania State University, University Park, PA, USA. [21]Perimeter Institute for Theoretical Physics, Waterloo, Ontario, Canada. [22]Physics Department, University of Bath, Claverton Down, UK. [23]Department of Astronomy, School of Physical Sciences, University of Science and Technology of China, Hefei, China. [24]Kavli Institute for Astrophysics and Space Research, Massachusetts Institute of Technology, Cambridge, MA, USA. [25]Center for Interdisciplinary Exploration and Research in Astrophysics (CIERA) and Department of Physics and Astronomy, Northwestern University, Evanston, IL, USA. [26]Korea Astronomy and Space Science Institute, Daejeon, Republic of Korea. [27]International Center for Advanced Studies and Instituto de Ciencias Físicas, ECyT-UNSAM and CONICET, Buenos Aires, Argentina. [28]SOAR Telescope/NSF's NOIRLab, La Serena, Chile. ✉e-mail: yuhan.yang@roma2.infn.it; eleonora.troja@uniroma2.it

a F150W F277W F444W

GRB 230307A

5 arcsec

G1

b **c** **d** **e** → G*

HST/F105W JWST/F277W JWST/F444W JWST/F277W
$T_0 + 29$ d $T_0 + 29$ d $T_0 + 29$ d $T_0 + 61$ d

f

log($F_{X,11h}/\phi_\gamma$)

221009A
060614 130427A
211211A
230307A ★

Short GRBs
Long GRBs

Projected physical offset (kpc)
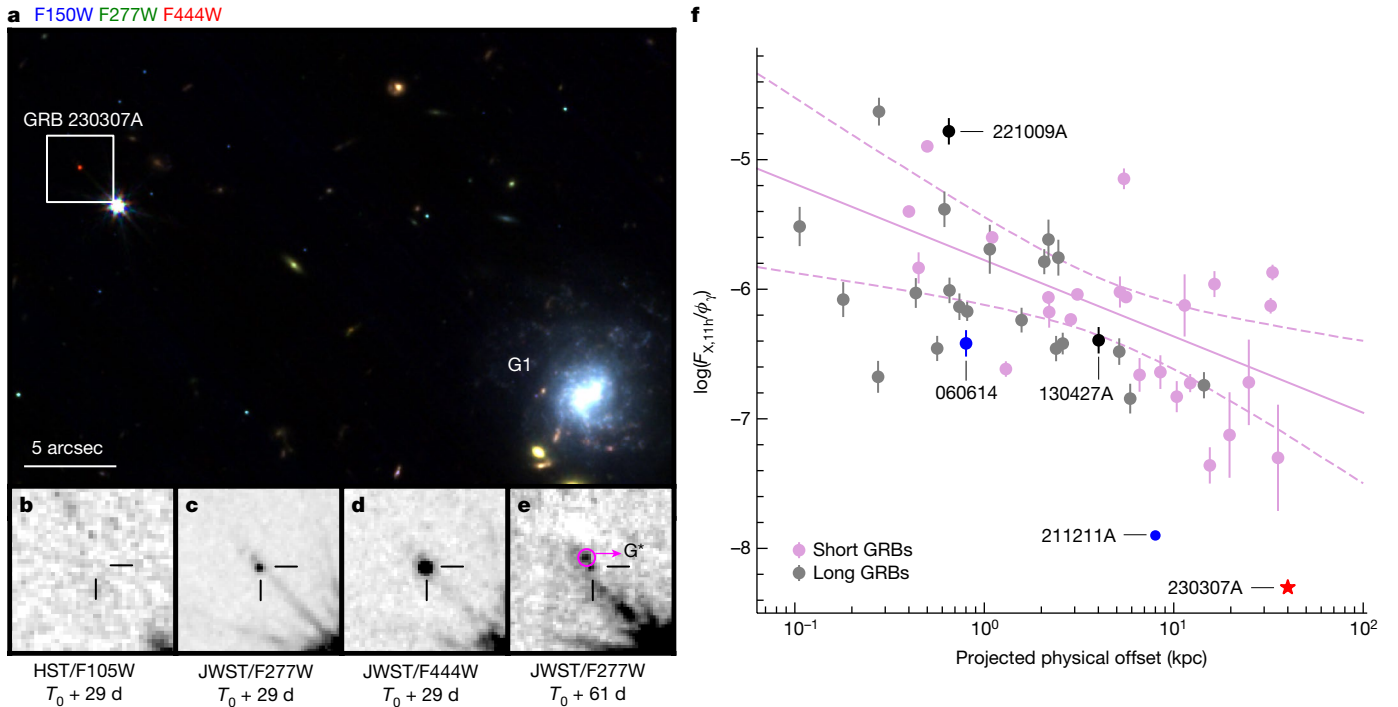
Fig. 1 | The environment of GRB 230307A. a, False-colour image combining three filters from JWST (F150W, F277W and F444W). The bright galaxy labelled by G1 is the most likely host galaxy at an offset of 40 kpc. **b**–**e**, Zoom-in on the transient location, corresponding to the white box in **a**. The field is shown in filters HST/F105W (**b**), JWST/F277W (**c**) and JWST/F444W (**d**) at $T_0 + 29$ d. The same field is shown in filter JWST/F277W at $T_0 + 61$ d (**e**). The transient has a very red colour in the near-simultaneous HST and JWST observations. The high-redshift galaxy G* is marked in the magenta circle in **e**. **f**, Ratio of 0.3–10 keV

X-ray flux at 11 h ($F_{X,11h}$) to the 15–150 keV gamma-ray fluence (ϕ_γ) versus the projected physical offset from the GRB host galaxy. The purple and grey data points represent short and long GRBs, respectively. The purple solid line and dashed lines indicate the best-fit model and the 95% CL for short GRBs, respectively. The bright long GRBs 221009A and 130427A are shown in black circles. Hybrid long GRBs 060614 and 211211A are shown in blue circles. GRB 230307A is marked by a red star, lying at the bottom of the distribution. Error bars are 1σ.

local origin in the Magellanic Clouds; (3) a nearby ($z \approx 0.0647$, corresponding to 291 Mpc; ref. 12) face-on spiral galaxy (G1 in Fig. 1a). Each of these three possibilities leads to extreme properties for GRB 230307A (Methods).

Further insights can be gleaned from the SED of the GRB counterpart, modelled with a power law plus a blackbody component (Methods). The results show that a thermal component exists in all spectra acquired >$T_0 + 1$ d (Fig. 2a–f). Until about $T_0 + 10$ d, this component shows a trend of decreasing temperature and increasing radius, which is consistent with an expanding fireball. By assuming homologous expansion and imposing that the velocity $v \approx (1 + z)R_{ph}/t$, where R_{ph} is the photosphere radius and t is time, cannot exceed the speed of light, we obtain $z < 0.43$ and rule out a high-redshift origin for GRB 230307A. In addition, at the putative distance of 291 Mpc, the temperature and radius of the thermal component match the evolution of the kilonova counterparts of GRB 170817A[13,14] and GRB 211211A[15] (Fig. 2h,i). This evidence provides additional support to the association between GRB 230307A and G1, and points to a new case of a kilonova following a long-duration GRB[15–20].

On the basis of this classification, we adopt an afterglow plus kilonova model to describe the multi-wavelength counterpart. The afterglow component describes the non-thermal emission arising from the relativistic ejecta and their interaction with the ambient medium[21]. The kilonova component instead accounts for the thermal emission arising from the sub-relativistic radioactive ejecta[2]. Multiple afterglow solutions are possible (Methods). However, regardless of the details of the explosion, the inclusion of a kilonova component represents a significant improvement based on the Bayesian information criterion (ΔBIC > 140). For our fiducial afterglow model (Fig. 3), we find strong evidence in favour of two kilonova components over the single kilonova component (ΔBIC = 19). The former component is produced by

fast moving ejecta ($v \approx 0.2c$, where c is the speed of light) with mass $M \approx 0.03\,M_\odot$ and opacity $\kappa \lesssim 3\,\mathrm{cm}^2\,\mathrm{g}^{-1}$ (3σ CL). This component mostly contributes to the optical and NIR emission over the first few days, then quickly fades away. The latter component is produced by slightly more massive ($M \approx 0.05\,M_\odot$), slower ($v \approx 0.03c$) ejecta with a significantly higher opacity ($\kappa \gtrsim 13\,\mathrm{cm}^2\,\mathrm{g}^{-1}$, 3$\sigma$ CL). This component becomes visible after about $T_0 + 10$ d and dominates the late-time emission. Its inclusion is mostly driven by the mid-infrared detections and their steep spectral profile ($\beta_{IR} \approx 3.2$), and relies on the assumption that the contribution of emission lines remains subdominant.

After estimating the contribution of the underlying non-thermal continuum, we derive the kilonova properties (Fig. 2). At approximately $T_0 + 7$ d, the effective temperature of the thermal component drops below 2,000 K (Fig. 2h), and the photospheric layer exhibits a tendency to recede into the inner regions (Fig. 2i). The velocity distribution as a function of mass can affect the evolution of the photosphere, but would produce a more gradual transition. A similar trend is instead observed in some type II supernovae during their hydrogen recombination phase[22]. In the case of a kilonova, the drop in effective temperature changes the ionization states of lanthanides and actinides, transitioning from singly ionized to neutral states, at a critical temperature of around 2,500 K (ref. 23). With a lower number of free electrons, the number of infrared bound–bound lines decreases considerably[24–26]. This causes a drop in the optical depth (Extended Data Fig. 6), accelerating the recession of the photosphere. The outer layers instead enter into an optically thin phase. This complex evolution is not accounted for by simple constant-opacity kilonova models and may explain why two kilonova components provide a better description of the dataset.

The kilonova bolometric luminosity is seen to rapidly decrease as $L_{bol} \propto t^{-2.7\pm0.4}$ (Fig. 2g), ranging from about 6×10^{39} erg s^{-1} at 29 d to about
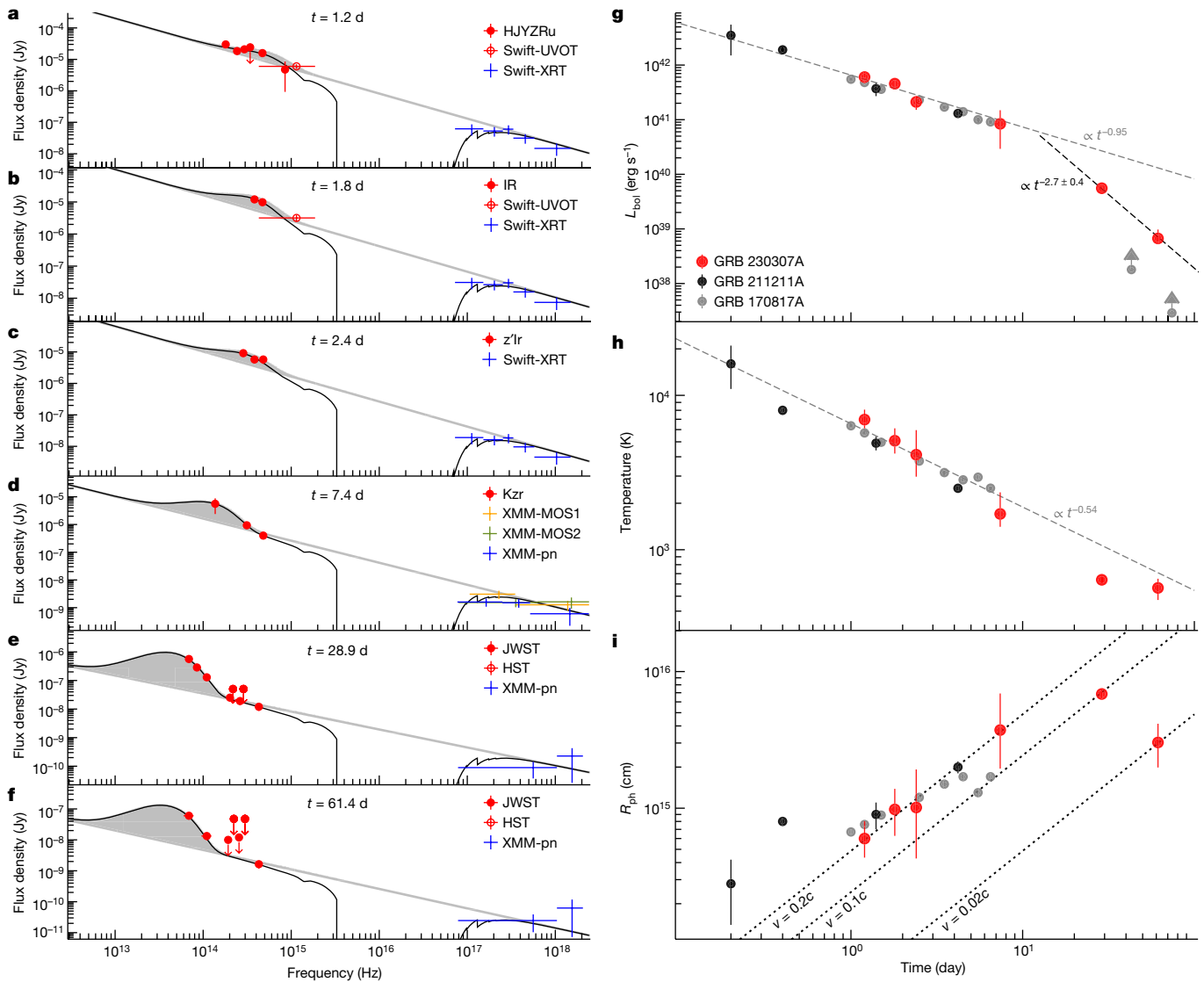
Fig. 2 | SED of the GRB counterpart. a–f, The observed spectra at different epochs (1.2 d (**a**), 1.8 d (**b**), 2.4 d (**c**), 7.4 d (**d**), 29 d (**e**) and 61 d (**f**) after the GRB) are fit with an empirical power law plus blackbody model (black solid thick lines). The grey shaded areas show the unabsorbed blackbody components and the grey thin solid lines show the power-law components. Different symbols represent different telescopes (JWST, HST) or detectors (Swift-UVOT, Swift-XRT, XMM-MOS1, XMM-MOS2, XMM-pn), and the filters of optical data points correspond from left to right according to the label (for example, HJYZRu).

g–i, The bolometric luminosity, effective temperature and photospheric radius of the thermal emission. GRB 211211A (black circles)[15] and GRB 170817A (grey circles)[13,14] are shown for comparison. The early bolometric luminosity and temperature (about 1–7 d) conform to simple power-law decay with slopes of −0.95 and −0.54, respectively[29]. The bolometric luminosity at late times decays with a steeper slope of −2.7 ± 0.4. The dotted lines in **i** indicate $R \approx \upsilon t/(1+z)$. Error bars and upper limits are the 1σ CL and the 3σ CL, respectively.

7×10^{38} erg s^{-1} at 61 d. A rapid decay of the luminosity was identified in the late-time observations of the kilonova AT2017gfo (refs. 13,14), and interpreted as a possible signature of short-lived heavy isotopes dominating the heating rate and thus the observed emission. However, in the case of AT2017gfo, the weak signal and limited coverage of the Spitzer data were not sufficient to characterize the spectral shape, and only placed lower limits on the true bolometric luminosity. In the case of GRB 230307A, the sensitivity and multi-colour coverage of the JWST and HST observations allow for better sampling. The data show that the ejecta is only partially optically thin and its late-time NIR luminosity is still dominated by photospheric emission of the inner layers. The evolution of the photosphere is consistent with adiabatic expansion and does not require a drop in the heating rate to explain the change in luminosity. Although this implies that no specific element can be identified based on temporal evolution, the fast decay of the luminosity can still inform us on the properties of this kilonova.

Predictions of the late-time evolution of a kilonova span a wide range of behaviours, depending on nuclear inputs and ejecta properties (for example, total mass, total energy, velocity distribution and ejecta composition). A common expectation is that, if translead nuclei such as ^{254}Cf are produced in the explosion, their decay products would deposit energy into the ejecta and cause the kilonova luminosity to flatten over time[27,28]. A hot central engine (for example, magnetar, pulsar or fall-back accretion) powering the lightcurve can also alter the late-time emission[8].

By comparing the bolometric lightcurve with different models (Fig. 4), we find that the efficient energy deposition of a long-lasting magnetar[8] or actinide fission fragments[27,28] is not consistent with the red colour and rapid decay of the bolometric lightcurve. A radioactive-powered kilonova containing r-process elements beyond the first peak (atomic mass number $A \gtrsim 85$) shows a better agreement with the data. This is because lighter elements have shorter lifetimes
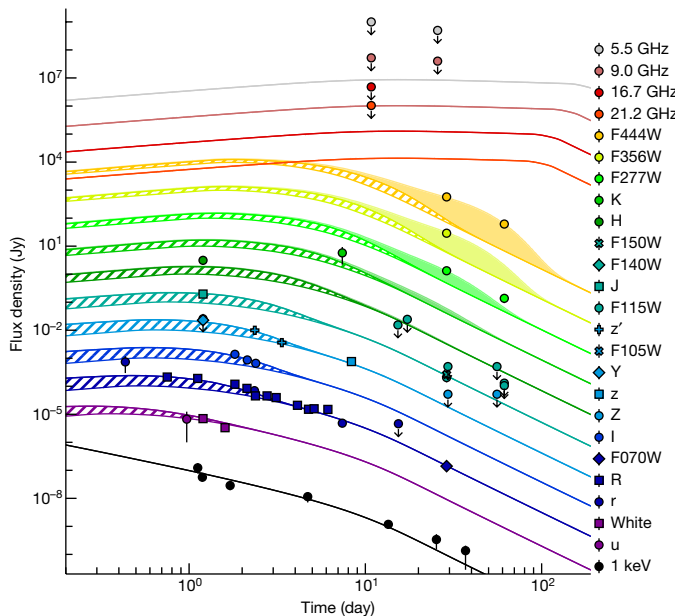
Fig. 3 | The multi-wavelength counterpart of GRB 230307A. The best-fit model to the multi-wavelength lightcurves. Except for the X-ray and the u/white bands, the nth lightcurve, when viewed from the bottom upwards, is vertically shifted by a factor of 10^n. The corresponding observed energy, filter and frequency are shown on the right side. Owing to the minor difference in effective wavelengths of some filters, we merged these observations into a single lightcurve. These lightcurves were fit by the emission contributed by a GRB afterglow (solid lines) and two-component kilonova (hatched and shaded areas). Error bars and upper limits are 1σ CL and 3σ CL, respectively.

and cannot provide sufficient radioactive power at these late epochs, resulting in a dimmer and cooler kilonova. The bolometric lightcurve, coupled with the observed evolution of the photospheric radius and the inferred high opacity, points to lanthanide production in the
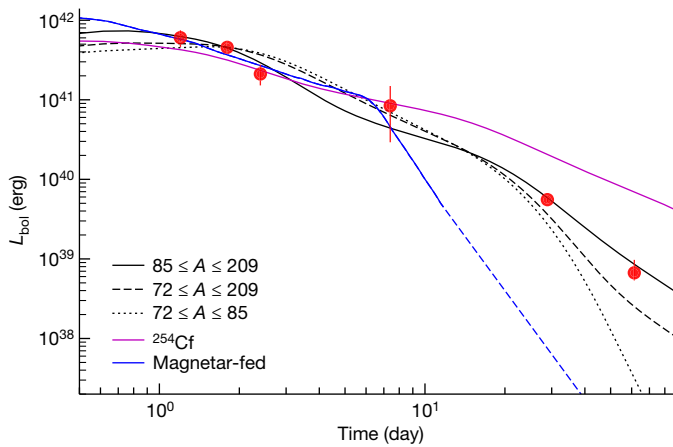

Fig. 4 | Comparison of the bolometric lightcurve with different models. The black lines are calculated using the model from ref. 6 with the solar r-process abundance pattern of different atomic mass ranges of $85 \leq A \leq 209$ (black solid line), $72 \leq A \leq 209$ (black dashed line) and $72 \leq A \leq 85$ (black dotted line). The ejecta parameters are $M_{ej} = 0.07\,M_\odot$, $v_{ej} = 0.1c$, $v_{ej,max} = 0.4c$ and $\beta_v = 1.5$. The opacity is $\kappa_1 = 0.6\,\mathrm{cm^2\,g^{-1}}$ and $\kappa_2 = 20\,\mathrm{cm^2\,g^{-1}}$ with the velocity threshold $0.15c$. The purple solid line illustrates the effects of efficient energy deposition by the spontaneous fission of ^{254}Cf, calculated for $M_{ej} = 0.05\,M_\odot$ and with effective heating rates from ref. 27. The blue line with dashed extrapolation illustrates the generic evolution of a magnetar-fed kilonova. We show the same model used to describe AT2017gfo (ref. 8) with $M_{ej} = 0.001\,M_\odot$, $v_{ej,max}/2 = 0.45c$, characteristic spindown luminosity $L_0 = 2 \times 10^{44}\,\mathrm{erg\,s^{-1}}$, gravitational-wave-dominated spindown timescale $t_{gw} = 495\,\mathrm{s}$ and magnetar lifetime $t_{cut} = 23\,\mathrm{d}$.

merger ejecta, and confirms kilonovae are a cosmic site of heavy r-process elements.

Online content

Any methods, additional references, Nature Portfolio reporting summaries, source data, extended data, supplementary information, acknowledgements, peer review information; details of author contributions and competing interests; and statements of data and code availability are available at https://doi.org/10.1038/s41586-023-06979-5.

1. Eichler, D., Livio, M., Piran, T. & Schramm, D. N. Nucleosynthesis, neutrino bursts and γ-rays from coalescing neutron stars. *Nature* **340**, 126–128 (1989).
2. Li, L.-X. & Paczyński, B. Transient events from neutron star mergers. *Astrophys. J.* **507**, L59–L62 (1998).
3. Freiburghaus, C., Rosswog, S. & Thielemann, F. K. R-process in neutron star mergers. *Astrophys. J.* **525**, L121–L124 (1999).
4. Korobkin, O., Rosswog, S., Arcones, A. & Winteler, C. On the astrophysical robustness of the neutron star merger r-process. *Mon. Not. R. Astron. Soc.* **426**, 1940–1949 (2012).
5. Barnes, J., Kasen, D., Wu, M.-R. & Martínez-Pinedo, G. Radioactivity and thermalization in the ejecta of compact object mergers and their impact on kilonova light curves. *Astrophys. J.* **829**, 110 (2016).
6. Hotokezaka, K. & Nakar, E. Radioactive heating rate of r-process elements and macronova light curve. *Astrophys. J.* **891**, 152 (2020).
7. Zhu, J.-P. et al. Long-duration gamma-ray burst and associated kilonova emission from fast-spinning black hole–neutron star mergers. *Astrophys. J.* **936**, L10 (2022).
8. Wollaeger, R. T. et al. Impact of pulsar and fallback sources on multifrequency kilonova models. *Astrophys. J.* **880**, 22 (2019).
9. Levan, A. et al. Heavy element production in a compact object merger observed by JWST. *Nature* https://doi.org/10.1038/s41586-023-06759-1 (2023).
10. Sun, H. et al. Magnetar emergence in a peculiar gamma-ray burst from a compact star merger. Preprint at https://arxiv.org/abs/2307.05689 (2023).
11. Bloom, J. S., Kulkarni, S. R. & Djorgovski, S. G. The observed offset distribution of gamma-ray bursts from their host galaxies: a robust clue to the nature of the progenitors. *Astron. J.* **123**, 1111–1148 (2002).
12. Freedman, W. L. et al. The Carnegie-Chicago Hubble Program. VIII. An independent determination of the Hubble constant based on the tip of the red giant branch. *Astrophys. J.* **882**, 34 (2019).
13. Waxman, E., Ofek, E. O. & Kushnir, D. Late-time kilonova light curves and implications to GW170817. *Astrophys. J.* **878**, 93 (2019).
14. Kasliwal, M. M. et al. Spitzer mid-infrared detections of neutron star merger GW170817 suggests synthesis of the heaviest elements. *Mon. Not. R. Astron. Soc.* **510**, L7–L12 (2022).
15. Troja, E. et al. A nearby long gamma-ray burst from a merger of compact objects. *Nature* **612**, 228–231 (2022).
16. Gehrels, N. et al. A new γ-ray burst classification scheme from GRB060614. *Nature* **444**, 1044–1046 (2006).
17. Yang, B. et al. A possible macronova in the late afterglow of the long-short burst GRB 060614. *Nat. Commun.* **6**, 7323 (2015).
18. Jin, Z.-P. et al. The light curve of the macronova associated with the long-short burst GRB 060614. *Astrophys. J.* **811**, L22 (2015).
19. Rastinejad, J. C. et al. A kilonova following a long-duration gamma-ray burst at 350 Mpc. *Nature* **612**, 223–227 (2022).
20. Yang, J. et al. A long-duration gamma-ray burst with a peculiar origin. *Nature* **612**, 232–235 (2022).
21. Ryan, G., van Eerten, H., Piro, L. & Troja, E. Gamma-ray burst afterglows in the multimessenger era: numerical models and closure relations. *Astrophys. J.* **896**, 166 (2020).
22. Valenti, S. et al. The diversity of type II supernova versus the similarity in their progenitors. *Mon. Not. R. Astron. Soc.* **459**, 3939–3962 (2016).
23. Barnes, J. et al. Kilonovae across the nuclear physics landscape: the impact of nuclear physics uncertainties on r-process-powered emission. *Astrophys. J.* **918**, 44 (2021).
24. Frey, L. H. et al. The Los Alamos Supernova Light-curve Project: computational methods. *Astrophys. J.* **204**, 16 (2013).
25. Fontes, C. J., Fryer, C. L., Hungerford, A. L., Wollaeger, R. T. & Korobkin, O. A line-binned treatment of opacities for the spectra and light curves from neutron star mergers. *Mon. Not. R. Astron. Soc.* **493**, 4143–4171 (2020).
26. Fontes, C. J., Fryer, C. L., Wollaeger, R. T., Mumpower, M. R. & Sprouse, T. M. Actinide opacities for modelling the spectra and light curves of kilonovae. *Mon. Not. R. Astron. Soc.* **519**, 2862–2878 (2023).
27. Zhu, Y. et al. Californium-254 and kilonova light curves. *Astrophys. J.* **863**, L23 (2018).
28. Holmbeck, E. M. et al. Superheavy elements in kilonovae. *Astrophys. J.* **951**, L13 (2023).
29. Waxman, E., Ofek, E. O., Kushnir, D. & Gal-Yam, A. Constraints on the ejecta of the GW170817 neutron star merger from its electromagnetic emission. *Mon. Not. R. Astron. Soc.* **481**, 3423–3441 (2018).

Article

Methods

Spectral energy distribution

We used XSPEC[30] to jointly fit the near-infrared, optical and X-ray SEDs at 1.2 d, 1.8 d, 2.4 d, 7.4 d, 28.9 d and 61.4 d (Fig. 2 and Extended Data Table 1). The observed optical data were converted to spectral files using the ftflx2xsp and uvot2pha tools within HEASOFT v6.31. Necessary data were extrapolated based on observations at nearby times and fit results of empirical lightcurve modelling (Extended Data Fig. 1 and Supplementary Information). The Galactic contribution was modelled using the model phabs for X-ray photoelectric absorption with a fixed hydrogen column density $N_H = 1.26 \times 10^{21}$ cm^{-2} (ref. 31), and the model redden for optical dust reddening[32] with fixed parameters $E(B - V) = 0.0758$ mag. Each SED was fit using a power-law model and a blackbody plus power-law model.

To constrain the presence of absorption systems at the GRB site, we include two additional components (zphabs and zdust), and varied the GRB distance scale up to a redshift $z < 0.5$. The fit with a power-law function yields tight constraints ($N_{H,z} < 2.5 \times 10^{21}$ cm^{-2} and $E(B - V)_z < 0.03$ mag at 1.2 d, 3σ CL), which disfavour models of GRB afterglows interacting with a dusty ambient medium[33]. However, the results show positive evidence for the inclusion of a blackbody component, starting as early as $T_0 + 1.2$ d. The best-fit parameters are listed in Extended Data Table 1. The addition of a thermal component loosens the constraints on the rest-frame reddening ($E(B - V)_z < 0.3$ mag), but its rapid onset remains inconsistent with the typical timescales of a thermal dust echo.

Constraints on the GRB distance scale

The GRB distance scale can leave a detectable imprint on its afterglow SED[34]; therefore, we include in our spectral fits three components that are sensitive to the GRB redshift: zphabs and zdust to model the absorption within the GRB host galaxy, and zigm to describe the effects of the intervening intergalactic medium. By selecting 100 redshift values uniformly distributed between 0 and 10, we mapped the variation of the test statistics (χ^2) as a function of redshift. Analysing this sample statistic allowed us to derive an upper limit of $z < 3.3$ at the 95% CL ($z < 4.1$ at the 99.9% CL). This result is mostly driven by the afterglow detection in the Swift UltraViolet and Optical Telescope (UVOT) filters u and white, which disfavour a high-redshift origin for GRB 230307A.

An even more stringent constraint can be placed using the properties of the blackbody component. From the fit, we derive its effective temperature T_{eff} and total observed flux, which can then be used to derive the bolometric luminosity L_{bol} and, assuming isotropy[35], the radius R_{ph} of the emitting surface for a certain redshift. By imposing that the expansion velocity $v \approx (1 + z)R_{ph}/t$ cannot exceed the speed of light, we obtain $z < 0.23$ and $z < 0.43$ from the SED at 1.2 d and 28.9 d, respectively.

Host-galaxy association

Here we explore the GRB environment using deep multi-colour imaging with HST (observed on 6 April 2023) and JWST (observed on 8 May 2023). A faint galaxy, referred to as G* (Fig. 1e), is located $0.24 \pm 0.01''$ from the explosion site and lies at $z \gtrsim 3.9$ based on the identification of a Hα emission line in its spectrum[36]. For this galaxy, we derive magnitudes F070W > 28.3 mag, F115W > 28.6 mag, F150W > 28.8 mag, F277W = 27.80 ± 0.15 mag and F444W = 28.15 ± 0.20 mag. Using the galaxy number counts from the JWST Prime Extragalactic Areas for Reionization and Lensing Science (PEARLS) project[37], we estimate a probability of chance coincidence[11] $P_{cc} \gtrsim 0.04$ using the F150W limit and $P_{cc} \approx 0.03$ using the F277W brightness.

A high-redshift origin would fit well within the classification of GRB 230307A as a long burst from a young stellar population. However, a redshift of $z \gtrsim 3.9$ is in tension with the limits from optical measurements ($z \lesssim 3.3$). Moreover, it would imply an unprecedented gamma-ray

energy release (about 10^{56} erg) followed by the onset of an extremely luminous and blue (rest-frame g-band absolute magnitude $M_g \approx -25.7$ at 7 d) transient, which has never been observed before. These considerations lead us to disfavour the association between the GRB and the distant galaxy G*.

The next most likely associations, in terms of posterior probability, are the Magellanic Clouds, which lie about 8° away from the GRB. By cross-correlating the catalogue of Swift bursts with the 10 brightest galaxies of the Local Group, we derive $P_{cc} \approx 0.05$ from the number of GRBs located within an 8° radius of any of those galaxies. However, a distance scale of only 50 kpc would drive GRB 230307A to the low-luminosity extreme of high-energy transients, consistent with the population of giant flares from soft gamma-ray repeaters, rather than GRBs. These giant flares are characterized by a quasi-thermal spectrum[38], which is not observed in GRB 230307A[39]. Unlike GRB 200425A, a candidate extragalactic giant flare[40], the low-energy photon index of GRB 230307A is about −1 (refs. 39,41), consistent with the non-thermal shape of GRBs. On the basis of the properties of its high-energy emission, a local origin for GRB 230307A is likewise disfavoured.

We perform a further exploration of the field surrounding GRB 230307A using our deep HST imaging to determine whether there is any other probable host. We computed the offset and HST/F140W photometry for all extended sources in the field. In Extended Data Fig. 2a, we show the probability of chance coincidence for a sample of nearby galaxies versus their distance from the GRB's localization. Although there exist a handful of additional galaxies within 10″ of the GRB position, there are no galaxies with similarly low probabilities. Owing to their faintness, each of these nearby galaxies has $P_{cc} > 0.25$ making them unlikely hosts. However, we identify a bright galaxy, hereafter G1 (Fig. 1a) at an offset of 30″ from the GRB localization. This galaxy has an infrared brightness of F140W ≈ 17.6 AB mag, which yields a $P_{cc} = 0.13$.

From the spectrum of G1 (Extended Data Fig. 2b), we derive a redshift of $z = 0.0647 \pm 0.0003$ for this galaxy based on Hα, Hβ, [O III], [N II] and [S II] emission lines. Therefore, we derive a nearby distance of 291 Mpc for G1, assuming a Lambda cold dark matter (ΛCDM) cosmology with a Hubble constant of $H_0 = 69.8$ km Mpc^{-1} s^{-1}, matter density parameter $\Omega_M = 0.315$ and dark-energy density parameter $\Omega_\Lambda = 0.685$ (refs. 12,42). The projected physical distance between the GRB and G1 would be about 40 kpc, among the largest values measured for GRBs[43], yet not unprecedented among short GRBs[44]. This seems consistent with the low X-ray flux to gamma-ray fluence ratio, also observed for GRB 211211A[15], and interpreted as an indication of a burst in a low-density environment[45]. However, even this interpretation is not free from uncertainties. In the case of GRB 230307A, the complex morphology of the gamma-ray lightcurve hardly resembles any of the previous examples of short GRBs with extended emission[39,46,47]. In addition, the probability of chance alignment between the GRB and the nearby galaxy G1 is $P_{cc} \approx 13\%$, a value generally considered too high for a reliable physical association.

In what follows, we consider G1 the most likely host for GRB 230307A, as, despite the high P_{cc}, the study of the afterglow SED points towards a low-redshift origin. The emission line properties of G1, namely, $L_{H\alpha} \approx 4 \times 10^{40}$ erg s^{-1} and log([N II])/Hα ≈ −0.6, provide estimates of the star formation rate (SFR) and metallicity of the galaxy, leading to SFR ≈ 0.2 $M_\odot$ yr^{-1} (refs. 48,49) and 12 + log(O/H) ≈ 8.6 (ref. 50).

We modelled the SED of G1 (Extended Data Table 2) using Prospector[51] with the same set-up as previously outlined in refs. 15,43,52. The data were first corrected for Galactic extinction along the line of sight[32]. Our best-fit model is shown in Extended Data Fig. 2c. We derive a stellar mass of $M_*/M_\odot = (2.4 \pm 0.9) \times 10^9$, an SFR of 0.20 ± 0.03 $M_\odot$ yr^{-1}, an intrinsic dust component with extinction $A_V = 0.20 \pm 0.02$ mag, a metallicity $Z/Z_\odot = 0.04^{+0.02}_{-0.01}$, and a mass-weighted stellar age of $2.8^{+2.2}_{-1.5}$ Gyr. The specific SFR ≈ 0.3 Gyr^{-1} is low for a long GRB host galaxy[53]. In fact, the host-galaxy properties as a whole (a low-mass galaxy, a low SFR and

an old stellar population) point towards a host galaxy that is entering quiescence[54]. This is quite similar to the host galaxy of GRB 211211A[15]. These similarities in the inferred host properties highlight a growing population of long-duration GRBs produced by the merger of two compact objects that may occur in similar galaxy types.

Prompt emission

Additional constraints on the GRB nature and its distance scale can be placed by a study of its prompt gamma-ray emission, shown in Extended Data Fig. 3. By converting the total fluence 3×10^{-3} erg cm^{-2} s^{-1} (10–1,000 keV)[10] to an isotropic energy ($E_{\text{iso},\gamma}$) and peak energy 1,255 keV into rest-frame $E_{\text{p}}(1 + z)$, the red dashed/solid line in Extended Data Fig. 3d illustrates GRB 230307A at different redshifts on the Amati-relation diagram[55]. For a wide range of typical GRB redshifts (0.25 < z < 1.7) GRB 230307A fits within the 1σ CL region of the standard distribution for long GRBs. For redshifts 0.01 < z < 0.06, it falls within the distribution of short GRBs (95% CL), whereas for even lower distances its isotropic energy approaches the soft gamma repeater (SGR) region, orders of magnitude lower than the weakest GRB[40]. Extended Data Fig. 3d shows that, if associated with the most likely host galaxy G* at $z \approx 3.9$, GRB 230307A would not only be the most energetic explosion ever observed, with an energy release an order of magnitude higher than that of GRB 221009A[56], but also deviate significantly from the general population of long GRBs. This provides us with additional evidence against a high-redshift origin. More plausible values ($E_{\gamma,\text{iso}} \approx 3 \times 10^{52}$ erg) are found assuming the distance of G1 at $z \approx 0.0647$. However, the GRB lies at the intersection between the two populations of bursts and the Amati diagram does not reduce the uncertainty in its classification.

Possible progenitors for GRB 230307A

The traditional classification of GRBs divides them into either long or short GRBs, based on a threshold of 2 s (ref. 57), which are generally associated with the collapse of massive stars and compact binary mergers, respectively. The merger of a white dwarf with a neutron star was also proposed to explain long GRBs without an associated supernova[20,58].

Massive star collapse. GRB 230307A is a burst of long duration, commonly associated with the collapse of a massive star. For a broad range of redshifts (0.25 < z < 1.7), the prompt emission of GRB 230307A fits within the Amati relation for long GRBs (Extended Data Fig. 3d), typically followed by a supernova. Using the prototypical SN1998bw[59] and the faint SN2022xiw[60] as templates and comparing them with the deep HST and JWST observations (Extended Data Fig. 4), we rule out the possibility of a supernova out to $z > 6.8$ and $z > 3.3$, respectively. Similarly, we eliminate fast-evolving supernovae, such as SN2005E[61] and SN2010X[62], at $z < 1$. Given the constraint $z < 0.43$ based on the evolution of the blackbody component, we find no plausible range of redshift and extinction values that could accommodate a massive star progenitor.

White dwarf–neutron star merger. The merger of a white dwarf–neutron star binary system can give rise to a GRB, provided the white dwarf is sufficiently massive (for example, GRB 211211A[20,63]). In such scenarios, the timescale of the GRB may extend beyond 2 s (refs. 64,65). The presence of neutron-rich matter[20] or materials undergoing radioactive decay[63] in the ejecta can contribute to additional optical excess[66], alongside the standard GRB afterglow. A neutron star–white dwarf merger is a plausible origin for GRB 230307A, and can explain many of its unusual properties, from the long duration to its environment. However, existing models for the associated optical transient[65,66] do not predict the rapid reddening observed in GRB 211211A and GRB 230307A, and match more closely the evolution of faint type Iax supernovae rather than kilonovae. On the basis of this fact, we tend to favour a compact binary merger as progenitor for GRB 230307A.

Compact binary merger. The merger of two compact objects, including neutron star–black hole and binary neutron star, comprising at least one neutron star, is known to produce a GRB and a short-lived red thermal transient, a kilonova[44]. Although it is challenging to conceive that the duration of GRBs originating from these mergers can extend to tens of seconds[67], this progenitor system best explains the properties of the GRB counterpart, such as its very red colour and rapid evolution, and its environment.

Multi-wavelength afterglow modelling

The non-thermal afterglow radiation that follows GRBs is best described as synchrotron emission from a population of shock-accelerated electrons. Multiple mechanisms contribute to shaping its evolution, the dominant being an external forward shock driven by the interaction of the GRB jet with the ambient medium. A reverse shock travelling backwards into the ejecta or long-lasting activity of the central engine may also contribute to the afterglow emission at early times[68].

Owing to the delayed localization of GRB 230307A, the available dataset does not allow us to unambiguously identify the origin of its early non-thermal emission. Therefore, we consider two possible options in our modelling: (1) forward-shock radiation is the only dominant component at all times, and (2) a reverse shock and/or central engine activity contributes at early times, with the forward shock dominating later on (>1 d). In the former case, we include all observational data (Dataset 1) in our fit, in the latter case we consider the Transiting Exoplanet Survey Satellite (TESS) and Australia Telescope Compact Array (ATCA) detections as upper limits (Dataset 2) to the forward-shock radiation.

Motivated by the results of the SED analysis, we fit these datasets with three models: (1) a simple forward-shock model, (2) a forward shock plus a kilonova component, and (3) a forward shock plus a two-component kilonova. To model the forward-shock emission, we utilized the Python package afterglowpy[21]. The free parameters are the isotropic-equivalent kinetic energy E_0, the circumburst density n_0, the fraction of burst kinetic energy in magnetic fields ε_{B} and in electrons ε_{e}, the power-law slope p of the electron energy distribution, the opening angle of the jet's core θ_{c}, and the electron participation fraction ξ_{N}. We applied a Gaussian structure for the GRB jet $E(\theta) = E_0 \exp(-\theta^2/2\theta_{\text{c}}^2)$ for $\theta \leq \theta_{\text{w}}$, where $\theta_{\text{w}} = 4\theta_{\text{c}}$ is the truncation angle. Owing to the extreme brightness of the prompt emission of GRB 230307A, we consider only an on-axis viewing angle $\theta_{\text{v}} \approx 0$ rad.

Regarding the kilonova component, we employed the isotropic model from ref. 69 in the Python package gwemlightcurves. The model assumes a grey opacity and describes the spectrum with a simple blackbody function. The free parameters in this model are the ejecta mass M_{ej}, its minimum velocity v_{ej}, velocity index β_v, opacity κ and electron fraction Y_{e}.

We fit the multi-wavelength observations based on the nested sampling algorithm implemented in the Python package pymultinest[70]. Considering that our data come from a variety of different telescopes, we included an additional 5% systematic uncertainty for all observations. The best-fit parameters, resulting χ^2 and BIC for each model and dataset are shown in Extended Data Tables 3 and 4 and Extended Data Fig. 5. The forward-shock model resulted in all cases in a poor description of the data (χ^2/dof > 4), and the addition of a kilonova component substantially improves the fit (χ^2/dof $\approx$ 2).

The fit to Dataset 1 is tightly constrained by the early optical lightcurve, which determines the peak flux and frequency of the forward-shock component. It requires a very early jet break (about 0.3 d) to accommodate the rapid decay of the broadband emission, thus stretching the physical parameters to unusual values. For these reasons, our fiducial model is based on the fit to Dataset 2 (Fig. 3). A two-component kilonova provides a better description (χ^2/dof $\approx$ 1.5) of the optical and infrared excess, capturing the full blue-to-red evolution of the transient, and the bright mid-infrared emission at late times.

Article

Opacity evolution

In transient explosions, the photosphere moves inwards in mass coordinates. But because the ejecta is moving rapidly outwards, the radius of the photosphere likewise increases. In type II supernovae, the opacity in the ejected hydrogen envelope is dominated by electron scattering. When these electrons recombine, the drop in opacity accelerates the recession of the photosphere in mass coordinates. The subsequent deceleration of the radial expansion is a key feature in understanding the plateau phase of type IIP supernovae[22]. In kilonovae, the opacity is dominated by bound–bound line transitions in lanthanides. Assuming local thermodynamic equilibrium, Extended Data Fig. 6 shows the different opacities for neodymium (Nd) as it evolves from singly ionized Nd, to neutral Nd. The number of lines in the 1–5 μm range drops considerably as it recombines, and the overall opacity will also decrease by roughly an order of magnitude. This sudden decrease in opacity will accelerate the inwards motion of the photosphere in mass coordinates, causing the radius of the photosphere to stop increasing, or even to recede. Non-thermal effects can alter these opacities in Extended Data Fig. 6, but the basic trends with decreasing temperature are likely to hold.

Data availability

Swift/XRT products are available from the online GRB repository (https://www.swift.ac.uk/xrt_products). Swift/UVOT data are available from Swift Data Access (https://www.swift.ac.uk/archive). X-shooter data are available from ESO Science Archive Facility (https://archive.eso.org). HST and JWST data are available from Mikulski Archive for Space Telescopes (https://mast.stsci.edu). Chandra data are available from Chandra Data Archive (https://cda.harvard.edu/chaser). The TESS lightcurve is available from TessTransients archive (https://tess.mit.edu/public/tesstransients). Gemini data are available from Gemini Observatory Archive (https://archive.gemini.edu). XMM-Newton data are available from XMM-Newton Science Archive (https://www.cosmos.esa.int/web/xmm-newton/xsa). Fermi/GBM data are available from Fermi Science Support Center (FSSC) FTP archive https://heasarc.gsfc.nasa.gov/FTP/fermi/data/gbm. All the processed data are available upon request to the corresponding authors. Source data are provided with this paper.

Code availability

Results can be reproduced using standard free analysis packages. Methods are fully described. Codes used to produce figures can be made available upon request.

30. Arnaud, K. A. XSPEC: the first ten years. In *Astronomical Data Analysis Software and Systems V, Conference Series* Vol. 101 (eds Jacoby, G. H. & Barnes, J.) 17–20 (Astronomical Society of the Pacific, 1996).
31. Willingale, R., Starling, R. L. C., Beardmore, A. P., Tanvir, N. R. & O'Brien, P. T. Calibration of X-ray absorption in our Galaxy. *Mon. Not. R. Astron.* **431**, 394–404 (2013).
32. Schlafly, E. F. & Finkbeiner, D. P. Measuring reddening with Sloan Digital Sky Survey stellar spectra and recalibrating SFD. *Astrophys. J.* **737**, 103 (2011).
33. Waxman, E., Ofek, E. O. & Kushnir, D. Strong NIR emission following the long duration GRB 211211A: dust heating as an alternative to a kilonova. Preprint at https://arxiv.org/abs/2206.10710 (2022).
34. Krühler, T. et al. The SEDs and host galaxies of the dustiest GRB afterglows. *Astron. Astrophys.* **534**, A108 (2011).
35. Sneppen, A. et al. Spherical symmetry in the kilonova AT2017gfo/GW170817. *Nature* **614**, 436–439 (2023).
36. Levan, A. J. et al. GRB 230307A: JWST NIRSpec observations, possible higher redshift. *GRB Coord. Netw. Circ.* No. 33580 (2023).
37. Windhorst, R. A. et al. JWST PEARLS. Prime Extragalactic Areas for Reionization and Lensing Science: project overview and first results. *Astron. J.* **165**, 13 (2023).
38. Chang, H.-Y & Kim, H.-I. On spatial distribution of short gamma-ray bursts from extragalactic magnetar flares. *J. Astron. Space Sci.* **19**, 1–6 (2002).
39. Dichiara, S. et al. A luminous precursor in the extremely bright GRB 230307A. *Astrophys. J.* **954**, L29 (2023).
40. Yang, J. et al. GRB 200415A: a short gamma-ray burst from a magnetar giant flare? *Astrophys. J.* **899**, 106 (2020).
41. Wang, Y., Xia, Z.-Q., Zheng, T.-C., Ren, J. & Fan, Y.-Z. A broken "α–intensity" relation caused by the evolving photosphere emission and the nature of the extraordinarily bright GRB 230307A. *Astrophys. J.* **953**, L8 (2023).
42. Planck Collaboration et al. Planck 2018 results. VI. Cosmological parameters. *Astron. Astrophys.* **641**, A6 (2020).
43. O'Connor, B. et al. A deep survey of short GRB host galaxies over z~0–2: implications for offsets, redshifts, and environments. *Mon. Not. R. Astron. Soc.* **515**, 4890–4928 (2022).
44. Jin, Z.-P. et al. A kilonova associated with GRB 070809. *Nat. Astron.* **4**, 77–82 (2020).
45. O'Connor, B., Beniamini, P. & Kouveliotou, C. Constraints on the circumburst environments of short gamma-ray bursts. *Mon. Not. R. Astron. Soc.* **495**, 4782–4799 (2020).
46. Norris, J. P. & Bonnell, J. T. Short gamma-ray bursts with extended emission. *Astrophys. J.* **643**, 266–275 (2006).
47. Dichiara, S. et al. Evidence of extended emission in GRB 181123B and other high-redshift short GRBs. *Astrophys. J.* **911**, L28 (2021).
48. Kennicutt, J. & Robert, C. Star formation in galaxies along the Hubble sequence. *Ann. Rev. Astron. Astrophys.* **36**, 189–232 (1998).
49. Chabrier, G. Galactic stellar and substellar initial mass function. *Publ. Astron. Soc. Pac.* **115**, 763–795 (2003).
50. Kobulnicky, H. A. & Kewley, L. J. Metallicities of 0.3<z<1.0 galaxies in the GOODS-North field. *Astrophys. J.* **617**, 240–261 (2004).
51. Johnson, B. D., Leja, J., Conroy, C. & Speagle, J. S. Stellar population inference with Prospector. *Astrophys. J.* **254**, 22 (2021).
52. O'Connor, B. et al. A tale of two mergers: constraints on kilonova detection in two short GRBs at z~0.5. *Mon. Not. R. Astron. Soc.* **502**, 1279–1298 (2021).
53. Palmerio, J. T. et al. Are long gamma-ray bursts biased tracers of star formation? Clues from the host galaxies of the Swift/BAT6 complete sample of bright LGRBs. III. Stellar masses, star formation rates, and metallicities at z>1. *Astron. Astrophys.* **623**, A26 (2019).
54. Whitaker, K. E., van Dokkum, P. G., Brammer, G. & Franx, M. The star formation mass sequence out to z=2.5. *Astrophys. J.* **754**, L29 (2012).
55. Amati, L. et al. Intrinsic spectra and energetics of BeppoSAX gamma-ray bursts with known redshifts. *Astron. Astrophys.* **390**, 81–89 (2002).
56. O'Connor, B. et al. A structured jet explains the extreme GRB 221009a. *Sci. Adv.* **9**, eadi1405 (2023).
57. Kouveliotou, C. et al. Identification of two classes of gamma-ray bursts. *Astrophys. J.* **413**, L101 (1993).
58. Becerra, R. L. et al. Deciphering the unusual stellar progenitor of GRB 210704A. *Mon. Not. R. Astron. Soc.* **522**, 5204–5216 (2023).
59. Clocchiatti, A., Suntzeff, N. B., Covarrubias, R. & Candia, P. The ultimate light curve of SN 1998bw/GRB 980425. *Astron. J.* **141**, 163 (2011).
60. Srinivasaragavan, G. P. et al. A sensitive search for supernova emission associated with the extremely energetic and nearby GRB 221009A. *Astrophys. J.* **949**, L39 (2023).
61. Perets, H. B. et al. A faint type of supernova from a white dwarf with a helium-rich companion. *Nature* **465**, 322–325 (2010).
62. Kasliwal, M. M. et al. Rapidly decaying supernova 2010X: a candidate ".Ia" explosion. *Astrophys. J.* **723**, L98–L102 (2010).
63. Zhong, S.-Q., Li, L. & Dai, Z.-G. GRB 211211A: a neutron star-white dwarf merger? *Astrophys. J.* **947**, L21 (2023).
64. Fryer, C. L., Woosley, S. E., Herant, M. & Davies, M. B. Merging white dwarf/black hole binaries and gamma-ray bursts. *Astrophys. J.* **520**, 650–660 (1999).
65. Kaltenborn, M. A. R. et al. Abundances and transients from neutron star-white dwarf mergers. *Astrophys. J.* **956**, 71 (2023).
66. Bobrick, A., Zenati, Y., Perets, H. B., Davies, M. B. & Church, R. Transients from one white dwarf–neutron star/black hole mergers. *Mon. Not. R. Astron. Soc.* **510**, 3758–3777 (2022).
67. Lu, W. & Quataert, E. Late-time accretion in neutron star mergers: implications for short gamma-ray bursts and kilonovae. *Mon. Not. R. Astron. Soc.* **522**, 5848–5861 (2023).
68. Gao, H., Lei, W.-H., Zou, Y.-C., Wu, X.-F. & Zhang, B. A complete reference of the analytical synchrotron external shock models of gamma-ray bursts. *New Astron. Rev.* **57**, 141–190 (2013).
69. Metzger, B. D. Kilonovae. *Living Rev. Relativ.* **23**, 1 (2019).
70. Buchner, J. et al. X-ray spectral modelling of the AGN obscuring region in the CDFS: Bayesian model selection and catalogue. *Astron. Astrophys.* **564**, A125 (2014).
71. Mereghetti, S., Rigoselli, M., Salvaterra, R., Tiengo, A. & Pacholski, D. P. XMM-Newton and INTEGRAL observations of the bright GRB 230307A: vanishing of the local absorption and limits on the dust in the Magellanic Bridge. *Astrophys. J.* **956**, 97 (2023).
72. Zhang, B. & Mészáros, P. Gamma-ray bursts: progress, problems & prospects. *Int. J. Mod. Phys. A* **19**, 2385–2472 (2004).

Author contributions Y.-H.Y. led the analysis of the prompt emission, SEDs and multi-wavelength lightcurves. E.T. initiated the project, coordinated the observations and their interpretation. B.O. led the study of the host galaxy. C.R.B., A.J.C.-T., Y.H., C.D.K., M.M., F.N., I.P.-G. and J.H.G. acquired and reduced the data of the SOAR telescope. R.R. led the analysis of the radio data. B.O. reduced the JWST data. E.T. and B.O. acquired and reduced the HST data. E.T., B.O. and Y.-H.Y. acquired and reduced the XMM-Newton data. E.T. and Y.-H.Y. reduced the Swift data. Y.-H.Y. reduced the TESS data. M.I., G.S.H.P., M.J., S.-W.C., H.C. and C.-U.L. acquired and reduced the data of the KMTNet and RASA36 telescopes. E.T., J.D., K.D. and A.K. acquired and reduced the data of the PRIME telescope. B.O., S.D. and J.H.G. acquired and reduced the data of the Gemini telescope. J.H.G. and E.T. reduced the data of the X-shooter telescope. Y.-H.Y., G.R., H.v.E. and Z.-G.D. contributed to afterglow modelling and their physical interpretation. Z.-K.P. contributed to possible progenitors. C.L.F. contributed to the interpretation of the data. Y.-H.Y., E.T., B.O. and C.L.F. wrote the paper, with contributions from all authors.

Competing interests The authors declare no competing interests.

Additional information
Supplementary information The online version contains supplementary material available at https://doi.org/10.1038/s41586-023-06979-5.
Correspondence and requests for materials should be addressed to Yu-Han Yang or Eleonora Troja.
Peer review information *Nature* thanks the anonymous reviewers for their contribution to the peer review of this work.
Reprints and permissions information is available at http://www.nature.com/reprints.
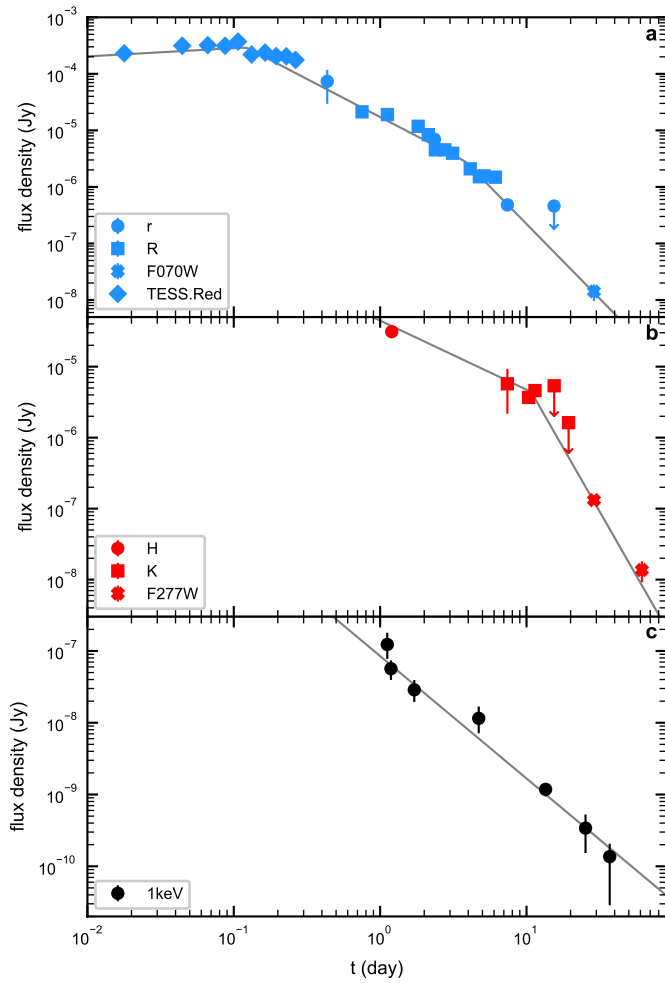
Extended Data Fig. 1 | Empirical model for the nIR, optical, and X-ray lightcurves. The lightcurves are modeled using PL segments, $F_\nu \propto t^{-\alpha}\nu^{-0.8}$. The gray lines represent the best-fit models. Different symbols indicate observations with different filters. Error bars and upper limits are 1σ c.l. and 3σ c.l., respectively.
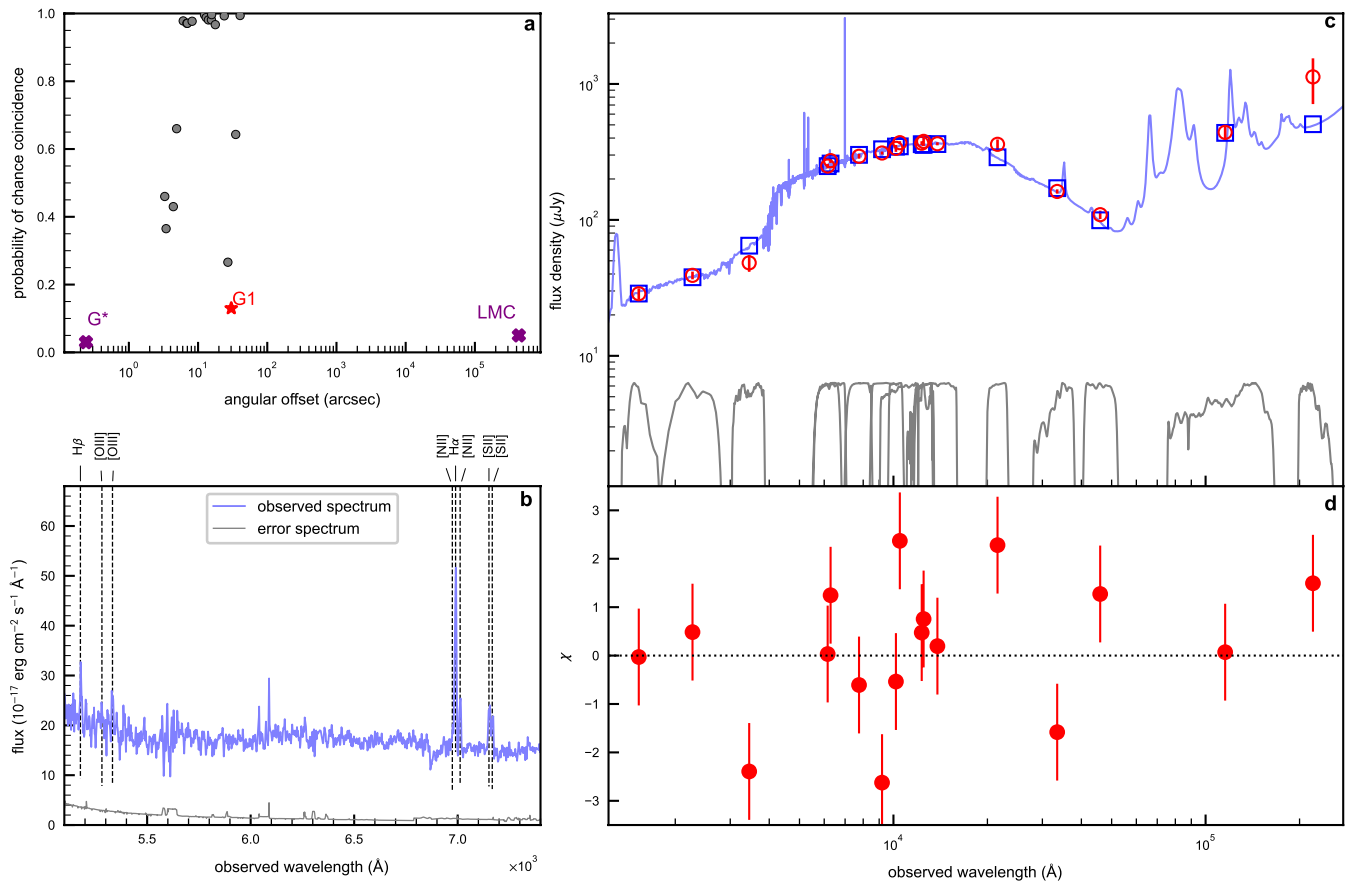
Extended Data Fig. 2 | Properties of the potential host galaxies. a, Probability of chance coincidence for galaxies in the field of GRB 230307A. Likely unrelated galaxies are displayed as gray circles. The candidate host galaxies G*, LMC (purple crosses) and G1 (red star) are highlighted. **b**, Optical spectrum of the bright galaxy G1. The observed spectrum is shown in blue and the error spectrum in black. Line identifications are made at $z = 0.0647 \pm 0.0003$.

The spectrum is smoothed with a Savitzky-Golay filter of two pixels for display purposes. **c,d**, Spectral energy distribution of the bright galaxy G1. The model SED (blue line) and model photometry (blue squares) derived using Prospector are compared to the observed photometry (red circles). Filter bandpasses are shown at the bottom of panel **c** in gray. Fit residuals are shown in **d**. Error bars represent 1σ uncertainties.
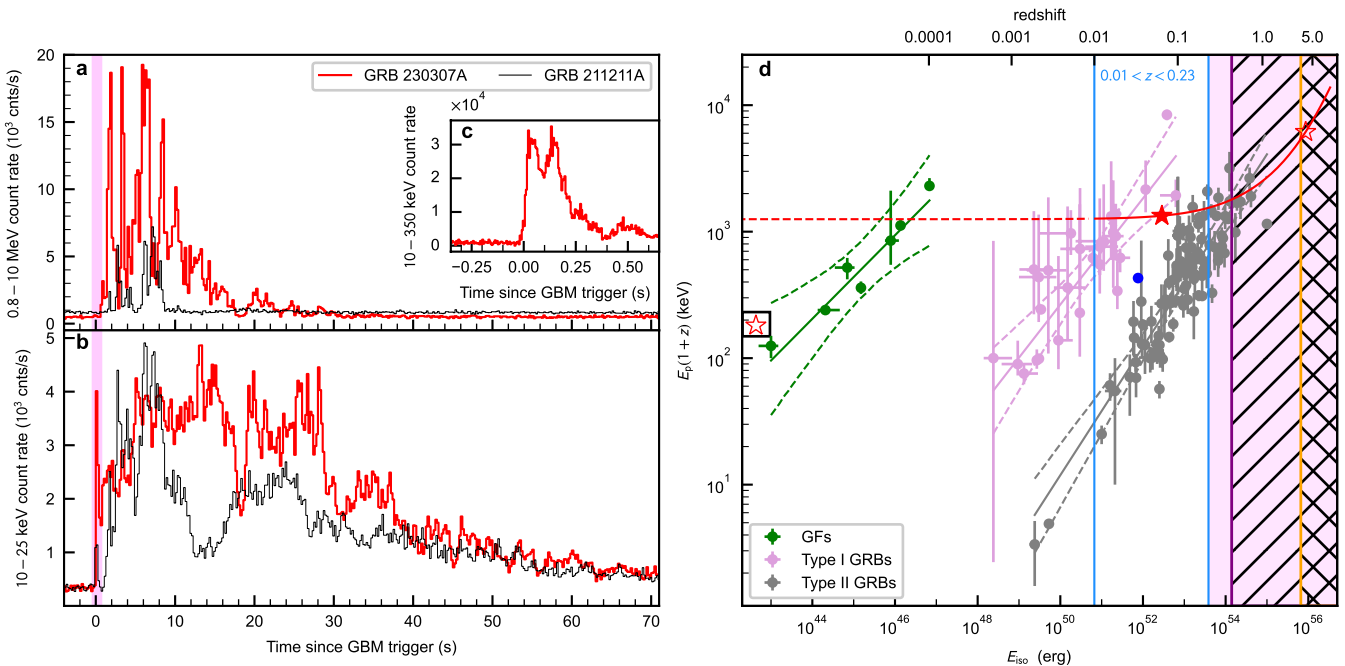
Extended Data Fig. 3 | Prompt emission properties of GRB 230307A.
a,b, Gamma-ray lightcurves of GRB 230307A (red) and GRB 211211A (dark) from *Fermi*/GBM in the energy range of 10–25 keV and 0.8–10 MeV with 0.2 s binsize. The purple shaded area roughly represents the time range of the initial pulse of the lightcurve, as depicted in the zoomed-in panel (**c**) with 5 ms binsize in the energy range 10–350 keV. **d**, The Amati-relation diagram. The plum/gray/green circles represent Type I (short) GRBs/Type II (long) GRBs/magnetar giant flares, and the corresponding color solid line and the area between dashed lines are the best-fit model and 95% c.l., respectively. GRB 230307A (whole burst) shifts following the red line when located at different redshifts. The red stars represent it at the three most probable host galaxies (G1, LMC and G*), while the GF is only reasonable when we treat the initial pulse as the main burst (zoom-in panel **c**). Hybrid GRB 211211A is shown in the blue circle. The purple shaded ($z > 0.23$)/hatched ($z > 0.43$) area is ruled out by the expansion velocity of the photosphere radius at $T_0 + 1.2$ d/28.9 d being limited to less than the speed of light. The orange hatched area is ruled out by the SED ($z \lesssim 3.3$). The red dashed line indicates the redshift where it departs from the 95% c.l. for the distribution of Type I GRBs. Error bars represent 1σ uncertainties.
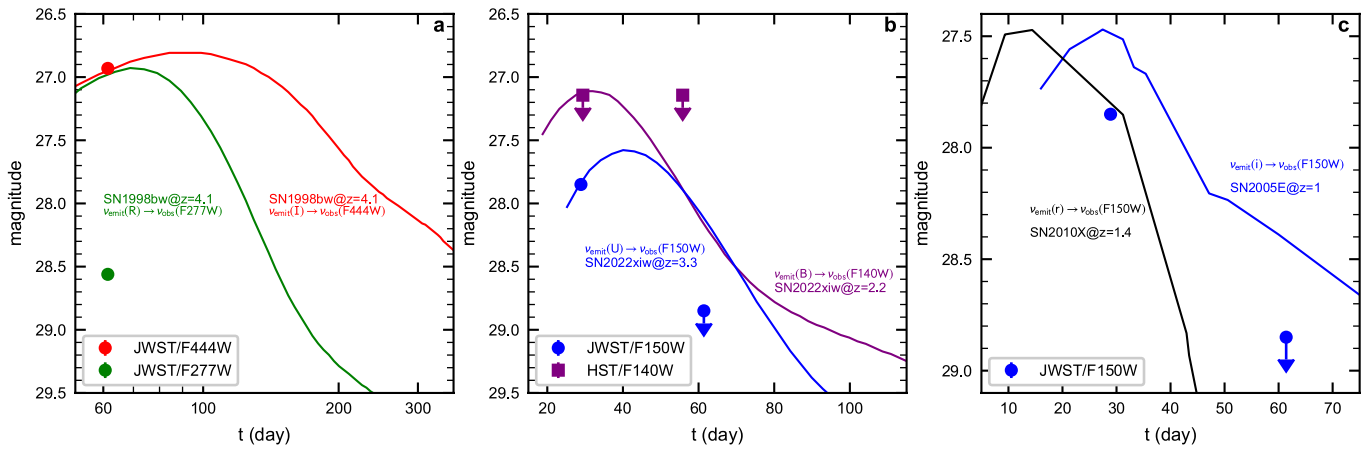
Extended Data Fig. 4 | Comparison of *JWST* and *HST* observations and supernova lightcurves at different redshifts. The lightcurves of SN1998bw/GRB 980425[59] (**a**), SN2022xiw/GRB 221009A[60] (**b**), SN2005E[61] and SN2010X[62] (**c**) are employed as references for typical GRB-SNe, bright GRB-SNe and fast-evolving SNe. Error bars and upper limits are 1σ c.l. and 3σ c.l., respectively.

a

b

Parameter	Prior	Posterior
FS		
$\log E_0$ (erg)	(50,60)	$53.87^{+1.34}_{-1.36}$
$\log n_0$ (cm^{-3})	(-6,2)	$-4.11^{+1.55}_{-1.20}$
$\log \theta_c$ (rad)	(-2,-0.5)	$-1.38^{+0.29}_{-0.27}$
$\log \varepsilon_e$	(-6,-0.3)	$-2.90^{+1.51}_{-1.36}$
$\log \varepsilon_B$	(-6,-0.3)	$-3.96^{+1.57}_{-1.34}$
p	(2.01,2.9)	$2.64^{+0.05}_{-0.05}$
$\log \xi_N$	(-5,0)	$-3.19^{+1.23}_{-1.13}$
2KN		
$\log M_{ej,1}$ (M$_\odot$)	(-3,-1)	$-1.56^{+0.14}_{-0.12}$
$\log v_{ej,1}$ (c)	(-1,-0.5)	$-0.72^{+0.13}_{-0.17}$
$\log \kappa_1$ (cm^{-2} g^{-1})	(-2,0.5)	$-0.24^{+0.26}_{-0.27}$
$\beta_{v,1}$	(1,5)	$3.09^{+1.14}_{-1.15}$
$Y_{e,1}$	(0.2,0.4)	$0.30^{+0.06}_{-0.06}$
$\log M_{ej,2}$ (M$_\odot$)	(-3,-1)	$-1.28^{+0.07}_{-0.06}$
$\log v_{ej,2}$ (c)	(-2,-1)	$-1.51^{+0.08}_{-0.09}$
$\log \kappa_2$ (cm^{-2} g^{-1})	(-0.5,2)	$1.66^{+0.22}_{-0.29}$
$\beta_{v,2}$	(1,5)	$2.25^{+1.01}_{-0.85}$
$Y_{e,1}$	(0.1,0.2)	$0.15^{+0.03}_{-0.03}$
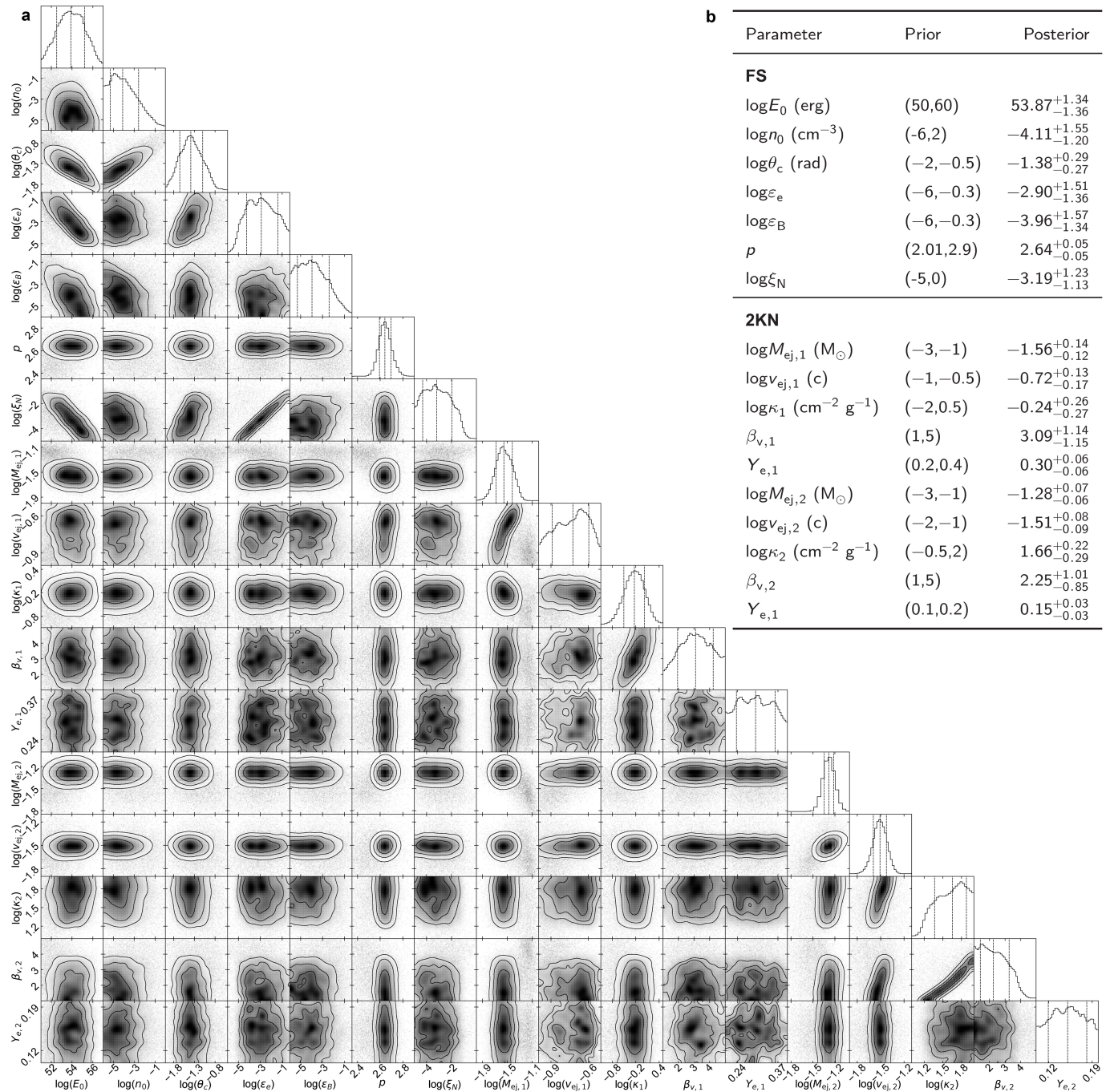
Extended Data Fig. 5 | Results for a forward shock plus two-component kilonova model for Dataset 2. a. Posterior probability distributions of parameters. **b**. The prior bounds and posterior medians for parameters. The values corresponding to the two kilonova components are denoted by the subscript 1 or 2. Uniform priors are employed for all parameters except for the electron index p, which is a truncated-Gaussian prior (2.46 ± 0.20) derived from the spectral index $\beta_X = 0.73 \pm 0.10$ (ref. 71) according to standard closure relations[72]. Error bars represent 1σ uncertainties.
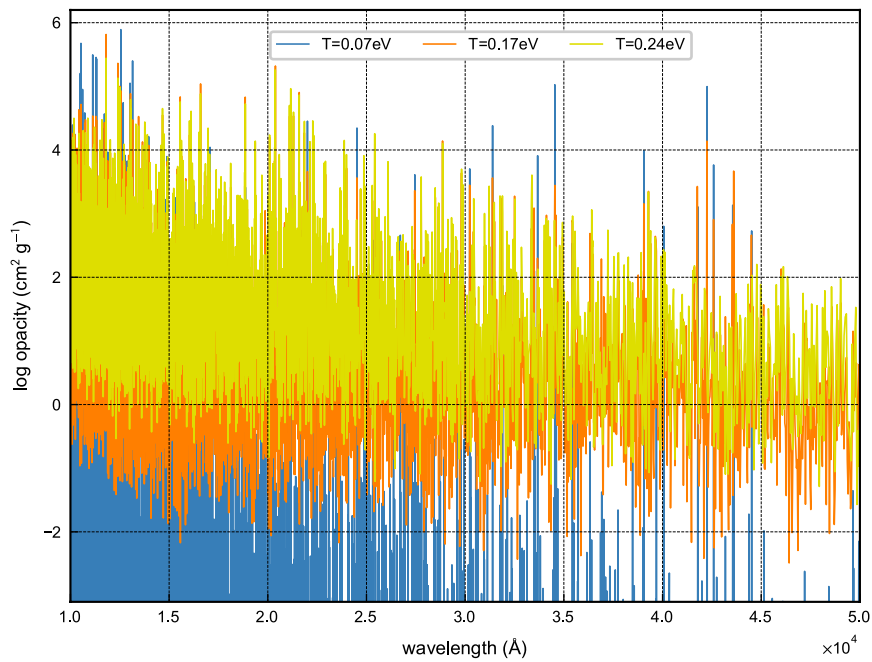
Extended Data Fig. 6 | Neodymium opacities in the 1–5 μm range at 3 temperatures: 0.24 eV, 0.17 eV and 0.07 eV. In local thermodynamic equilibrium, these correspond to ionization fractions of 1.0 ($T = 0.24$ eV), 0.886 ($T = 0.17$ eV) and 10^{-6} ($T = 0.07$ eV). The material begins to recombine between 0.24 and 0.17 eV (2,000–2,500 K). As it recombines, the number of bound-bound lines in the 1–5 μm range decreases significantly, causing a drop in the opacity.

Extended Data Table 1 | Infrared/optical/X-ray joint spectral fit results for power-law or afterglow plus blackbody model

t	β_{OX}	T_{eff}	L_{bol}	R_{ph}	ΔStat
(day)		(K)	(erg s^{-1})	(cm)	
PL+BB					
1.2		$6,966^{+1,113}_{-864}$	$6.03^{+1.43}_{-1.42} \times 10^{41}$	$6.00^{+2.04}_{-1.65} \times 10^{14}$	
1.8	$0.80^{+0.02}_{-0.02}$	$5,082^{+1,032}_{-885}$	$4.56^{+0.79}_{-0.80} \times 10^{41}$	$9.79^{+4.07}_{-3.52} \times 10^{14}$	38.2
2.4		$4,125^{+1,827}_{-1,152}$	$2.11^{+0.64}_{-0.60} \times 10^{41}$	$1.01^{+0.91}_{-0.58} \times 10^{15}$	
7.4		$1,705^{+647}_{-297}$	$8.40^{+6.49}_{-5.48} \times 10^{40}$	$3.73^{+3.18}_{-1.78} \times 10^{15}$	
28.9	$0.63^{+0.07}_{-0.05}$	638^{+21}_{-21}	$5.56^{+0.45}_{-0.39} \times 10^{39}$	$6.85^{+0.54}_{-0.53} \times 10^{15}$	609.3
61.4		565^{+83}_{-93}	$6.69^{+3.04}_{-1.32} \times 10^{38}$	$3.03^{+1.12}_{-1.04} \times 10^{15}$	
AF+BB					
1.2		$5,018^{+572}_{-598}$	$5.78^{+0.80}_{-0.90} \times 10^{41}$	$1.13^{+0.27}_{-0.28} \times 10^{15}$	
1.8		$6,200^{+2,847}_{-2,377}$	$4.68^{+1.69}_{-1.03} \times 10^{41}$	$6.67^{+6.24}_{-5.17} \times 10^{14}$	
2.4		$3,882^{+2,064}_{-2,264}$	$1.77^{+1.00}_{-1.00} \times 10^{41}$	$1.05^{+1.15}_{-1.26} \times 10^{15}$	
28.9		612^{+26}_{-28}	$5.60^{+0.68}_{-0.65} \times 10^{39}$	$7.46^{+0.79}_{-0.83} \times 10^{15}$	
61.4		579^{+100}_{-135}	$6.87^{+4.13}_{-1.92} \times 10^{38}$	$2.92^{+1.34}_{-1.42} \times 10^{15}$	

Errors represent the 1σ uncertainties. The bolometric luminosity and photosphere radius are calculated based on the assumed luminosity distance D_L =291 Mpc. The fit statistics between the power-law (PL) model and PL plus blackbody (BB) model, ΔStat=Stat$_{PL}$ – Stat$_{PL+BB}$, represents the improvement in spectral fit by an additional BB component. The afterglow components are generated based on our fiducial model.

Extended Data Table 2 | Photometry of the bright galaxy G1

Date	Telescope	Filter	Magnitude
Archival	*GALEX*	*FUV*	20.84 ± 0.19
Archival	*GALEX*	*NUV*	20.43 ± 0.12
1.0	UVOT	*u*	20.06 ± 0.24
7.4	Gemini	*r*	17.98 ± 0.05
8.3	Gemini	*z*	17.76 ± 0.03
17.3	Gemini	*J*	17.54 ± 0.04
2.1	SAAO	*r*	18.08 ± 0.05
2.1	SAAO	*i*	17.85 ± 0.05
Archival	VISTA	*Y*	17.66 ± 0.07
Archival	VISTA	*J*	17.51 ± 0.09
Archival	VISTA	K_s	17.53 ± 0.10
29.4	*HST*	*F105W*	17.56 ± 0.01
29.4	*HST*	*F140W*	17.55 ± 0.01
Archival	WISE	*W1*	18.38 ± 0.04
Archival	WISE	*W2*	18.80 ± 0.08
Archival	WISE	*W3*	17.29 ± 0.15
Archival	WISE	*W4*	16.27 ± 0.50

Magnitudes are reported in the AB system and are not corrected for Galactic extinction. Errors represent the 1σ uncertainties.

Article

Extended Data Table 3 | Summary of model fitting results

Model	Dataset 1		Dataset 2	
	χ^2/dof	BIC	χ^2/dof	BIC
FS	487.7/63	517.4	286.2/63	315.9
FS+KN	198.4/58	249.4	118.7/58	169.7
FS+2KN	163.5/53	235.7	78.8/53	151.0

The fit statistics for the three different models analyzed in this work: a forward shock (FS) model, a forward shock and a kilonova (FS+KN), and a forward shock with a two-component kilonova (FS+2KN). All available observational data are included in Dataset 1. Compared to Dataset 1, the TESS and ATCA detections are treated as upper limits in Dataset 2. The best-fit χ^2 divided by the degree of freedom (dof) and BIC obtained from all model fittings are compared.

Extended Data Table 4 | Model parameters, prior bounds and posterior medians from modeling of Dataset 1 and Dataset 2 with a forward shock (FS) plus a kilonova model (KN)

Parameter	Prior	Posterior	
		Dataset 1	Dataset 2
FS			
$\log E_0$ (erg)	(50,60)	$50.70^{+0.20}_{-0.17}$	$54.26^{+1.41}_{-1.66}$
$\log n_0$ (cm^{-3})	(-6,2)	$1.87^{+0.09}_{-0.18}$	$-4.35^{+1.75}_{-1.07}$
$\log \theta_c$ (rad)	$(-2,-0.5)$	$-0.75^{+0.05}_{-0.05}$	$-1.49^{+0.35}_{-0.25}$
$\log \varepsilon_e$	$(-6,-0.3)$	$-0.42^{+0.09}_{-0.17}$	$-3.01^{+1.64}_{-1.54}$
$\log \varepsilon_B$	$(-6,-0.3)$	$-3.59^{+0.19}_{-0.17}$	$-4.03^{+1.53}_{-1.30}$
p	(2.01,2.9)	$2.11^{+0.03}_{-0.03}$	$2.64^{+0.05}_{-0.05}$
$\log \xi_N$	(-5,0)	$-1.41^{+0.12}_{-0.17}$	$-2.99^{+1.38}_{-1.24}$
KN			
$\log M_{ej}$ (M$_\odot$)	$(-3,-1)$	$-1.20^{+0.03}_{-0.03}$	$-1.29^{+0.04}_{-0.04}$
$\log v_{ej}$ (c)	$(-2,-0.3)$	$-1.23^{+0.04}_{-0.04}$	$-1.28^{+0.07}_{-0.07}$
$\log \kappa$ (cm^{-2} g^{-1})	$(-1,2)$	$-0.66^{+0.57}_{-0.08}$	$0.66^{+0.14}_{-0.15}$
β_v	(1,5)	$1.10^{+2.19}_{-0.07}$	$3.69^{+0.73}_{-0.80}$
$Y_{e,1}$	(0.1,0.5)	$0.30^{+0.13}_{-0.13}$	$0.30^{+0.12}_{-0.13}$

A truncated-Gaussian prior distribution with mean 2.46 and standard deviation 0.20 is used for electron index p, while uniform priors are employed for other parameters. Errors represent the 1σ uncertainties.